Nanostructure of cellulose microfibrils in spruce wood

Anwesha N. Fernandes[a], Lynne H. Thomas[b], Clemens M. Altaner[c], Philip Callow[d], V. Trevor Forsyth[d,e], David C. Apperley[f], Craig J. Kennedy[g], and Michael C. Jarvis[h,1]

[a]Centre for Plant Integrative Biology, University of Nottingham, Sutton Bonnington Campus, Leicestershire LE12 5RD, United Kingdom; [b]Department of Chemistry, University of Bath, Claverton Down, Bath BA2 7AY, United Kingdom; [c]New Zealand School of Forestry, University of Canterbury, Christchurch 8140, New Zealand; [d]Institut Laue-Langevin, 38042 Grenoble Cedex 9, France; [e]Environment, Physical Sciences, and Applied Mathematics/Institute for Science and Technology in Medicine, Keele University, Staffordshire ST5 5BG, United Kingdom; [f]Chemistry Department, Durham University, Durham DH1 3LE, United Kingdom; [g]Historic Scotland, Longmore House, Salisbury Place, Edinburgh EH9 1SH, United Kingdom; and [h]School of Chemistry, Glasgow University, Glasgow G12 8QQ, United Kingdom

Edited* by Chris R. Somerville, University of California, Berkeley, CA, and approved September 19, 2011 (received for review June 6, 2011)

The structure of cellulose microfibrils in wood is not known in detail, despite the abundance of cellulose in woody biomass and its importance for biology, energy, and engineering. The structure of the microfibrils of spruce wood cellulose was investigated using a range of spectroscopic methods coupled to small-angle neutron and wide-angle X-ray scattering. The scattering data were consistent with 24-chain microfibrils and favored a "rectangular" model with both hydrophobic and hydrophilic surfaces exposed. Disorder in chain packing and hydrogen bonding was shown to increase outwards from the microfibril center. The extent of disorder blurred the distinction between the I alpha and I beta allomorphs. Chains at the surface were distinct in conformation, with high levels of conformational disorder at C-6, less intramolecular hydrogen bonding and more outward-directed hydrogen bonding. Axial disorder could be explained in terms of twisting of the microfibrils, with implications for their biosynthesis.

crystallinity | infrared | deuterium exchange | nuclear magnetic resonance | spin diffusion

Cellulose makes up about half of the mass of wood, and wood cellulose is therefore more abundant than any other material in the biosphere (1). Cellulose synthesis is the key to the living world's buffering of atmospheric carbon dioxide levels and its utilization will be crucial to our efforts to find substitutes for fossil fuels (2). Nevertheless we have much to learn about the nature of cellulose and about how its structure relates to its function. Wood cellulose is composed of long microfibrils, each a few nanometers in thickness (3). These microfibrils contain both ordered and disordered components (4–6), but their structure is not known in detail.

Within each microfibril there are domains that conform approximately (4, 7, 8) to the cellulose Iα and Iβ forms found in much more crystalline algal and tunicate celluloses (9–11). Distinguishing these two forms is difficult in wood, but it has been suggested that cellulose resembling the Iβ form predominates in softwoods (8, 12). Also present are partially ordered cellulose chains (7) and chains that differ conformationally from crystalline cellulose (5, 6, 13). Other polysaccharides, particularly glucomannans, may be closely enough associated with the microfibrils to be considered as a part of their structure (14, 15).

There is evidence that the cellulose microfibrils of conifer wood are assembled into aggregates in the region of 10–20 nm across (16). In cross-section the wood cell wall is so dense that these microfibril aggregates are not readily visible, but they have been imaged by atomic force microscopy (17) and electron tomography (3), which showed their structures to be somewhat irregular and interspersed to a limited degree with other polymers. In SEM images of transversely fractured wood the fracture planes cut cleanly across each microfibril aggregate but also run between aggregates for short distances, giving a stepped topography (18). In mechanical terms, therefore, the microfibril aggregate appears to be the basic cohesive unit of the dry wood cell wall in the sense that it does not readily fray into its constituent microfibrils during fracture.

The above description does not include precise dimensions of microfibrils and their aggregates, nor the number of chains in each microfibril, nor the disposition of its component crystalline and noncrystalline fractions. These details have been elusive. The determination of microfibril diameters in wood has been addressed frequently by a variety of techniques, particularly wide-angle X-ray scattering (WAXS) and solid-state ^{13}C NMR (19–22). However each technique has drawbacks and agreement has not been generally good. Diameters suggested have ranged from 2.2 nm to 3.6 nm (20, 23). These upper and lower limits correspond to about 12 and 32 chains ($\pi r^2/0.317$) if it is assumed that the wood microfibrils are approximately circular in cross-section and each chain occupies 0.317 nm^2 as in cellulose Iβ (9).

EM images suggest that each microfibril is synthesized by a terminal complex that takes the shape of a six-lobed "rosette" (24). Each terminal complex contains multiple cellulose synthase subunits. Distinct groups of cellulose synthases participate in the synthesis of primary (growing) and secondary (woody) cell walls (25). If it is correct that one terminal complex makes one microfibril, it would seem to follow that microfibrils synthesized during primary and secondary cell-wall formation should contain fixed numbers of cellulose chains, divisible by six. A 36-chain model is frequently suggested (25), although the evidence on which this was originally based is very indirect (26) and a 36-chain microfibril would be larger than the spectroscopic and WAXS evidence suggests, about 3.8 nm diameter ($2\sqrt{(36\times0.317)/\pi}$) or 3×5 nm (27).

Microfibrils synthesized in a matrix with few noncellulosic polymers, as in cotton, flax, and angiosperm tension wood, have considerably larger and apparently variable dimensions (20, 28, 29) suggesting coalescence of newly synthesized microfibrils. Microfibrils appeared to split apart along the 002 crystal plane when subjected to vigorous acoustic degradation (30) and there is evidence that in some fruits the primary-wall microfibrils are less than 2 nm thick in their native state (31). When the diameter of wood microfibrils has been explored by a single technique, its variability has been small (19, 21) and might be explained by contributions from noncellulosic material. Thus although in certain circumstances the number of chains in a microfibril appears to vary and to differ from the number synthesized by each terminal complex (27), evidence that this applies also to normal wood microfibrils is lacking.

Author contributions: A.N.F., L.H.T., C.M.A., P.C., V.T.F., D.C.A., and M.C.J. designed research; A.N.F., L.H.T., C.M.A., P.C., V.T.F., D.C.A., and M.C.J. performed research; C.M.A. contributed new reagents/analytic tools; A.N.F., L.H.T., C.M.A., P.C., V.T.F., D.C.A., C.J.K., and M.C.J. analyzed data; and M.C.J. wrote the paper.

The authors declare no conflict of interest.

*This Direct Submission article had a prearranged editor.

[1]To whom correspondence should be addressed. E-mail: mikej@chem.gla.ac.uk.

See Author Summary on page 18863.

This article contains supporting information online at www.pnas.org/lookup/suppl/doi:10.1073/pnas.1108942108/-/DCSupplemental.

With these uncertainties, the number of chains in a microfibril is relevant to our understanding of cellulose biosynthesis, which is in turn closely entwined with the development of plant form (32) and function (33). The diameter of the cellulose fibrils and the proportion of crystalline material are key inputs into our understanding of the mechanical performance of cellulose (34–36) and into calculations of the strength of wood, textile fibers, and cellulose-based nanocomposite materials (37, 38). In addition cellulose "crystallinity" and aggregation control accessibility to glucanase enzymes (39) and are thus important but rather poorly defined questions in the technology of liquid biofuel production from cellulosic biomass.

Here we explore the questions of microfibril structure, diameter, and aggregation in spruce wood, from multiple experimental directions. Using WAXS in combination with small-angle neutron scattering, we constrained the microfibril dimensions within limits that are tighter than has previously been possible. We used deuteration-FTIR experiments to identify cellulose chains on microfibril surfaces accessible to water and two independent ^{13}C NMR approaches to characterize their conformation and location.

Results

Lateral Packing and Diameter of Microfibrils: Small-Angle Neutron Scattering (SANS). Microfibrils close-packed in a regular array would be expected to diffract radiation transverse to the microfibril axis, at angles an order of magnitude smaller than in conventional diffraction from crystal planes. It may be asked whether such small-angle scattering is expected from microfibril arrays with less ordered packing. In scattering models developed for collagen (40) and adapted for celery cellulose (41) a coherent scattering peak of this kind was constructed for a partially ordered array of parallel microfibrils with a range of spacings based on a modified Lennard-Jones function, the lower limit being fixed by contact and higher-order peaks being absent due to mingling with the contribution of the shape of the individual microfibrils (the form function) (41).

The smallest spacing would then be the center-to-center distance between microfibrils touching one another. Coherent small-angle scattering of X-rays has been observed from the loosely arrayed microfibrils of primary-wall cellulose in celery collenchyma (41). It was necessary to separate this interference contribution from that of the form function, but the q value of the interference peak provided a more direct measure of physical diameter than either the Scherrer dimensions calculated from WAXS data or the surface:volume ratios from spectroscopic measurements.

This approach does not work for wood. X-ray scattering from wood in its native state is dominated by the form function. Jakob, et al. (23) succeeded in extracting an interference contribution numerically, but it was small and difficult to characterize. From this observation it may be concluded that either the packing of wood microfibrils is too irregular to diffract strongly (42) or there is insufficient X-ray contrast between the microfibrils and any interstitial material (23). Intriguingly, an equatorial X-ray diffraction peak like that from celery cellulose microfibrils was observed after spruce wood was vigorously oxidized by chlorite/acetic acid (42).

Neutron and X-ray scattering intensities show different dependence on composition. The total neutron scattering cross-section of cellulose calculated from its elemental composition lies between those of H_2O and D_2O, and matches a 35:65 D_2O:H_2O mixture (43). It would therefore be predicted that if either H_2O or D_2O penetrated between regularly packed cellulose microfibrils they would provide neutron scattering contrast and would allow any interference contribution to be observed. Fig. 1 shows that Sitka spruce wood, saturated with either H_2O or D_2O, gave a strong lateral SANS peak centered on $q = 1.6$ nm^{-1}, quite similar to that observed for celery cellulose by SAXS (44). As predicted from elemental composition, the intensity of the interference peak was greater for wood saturated with D_2O than with H_2O

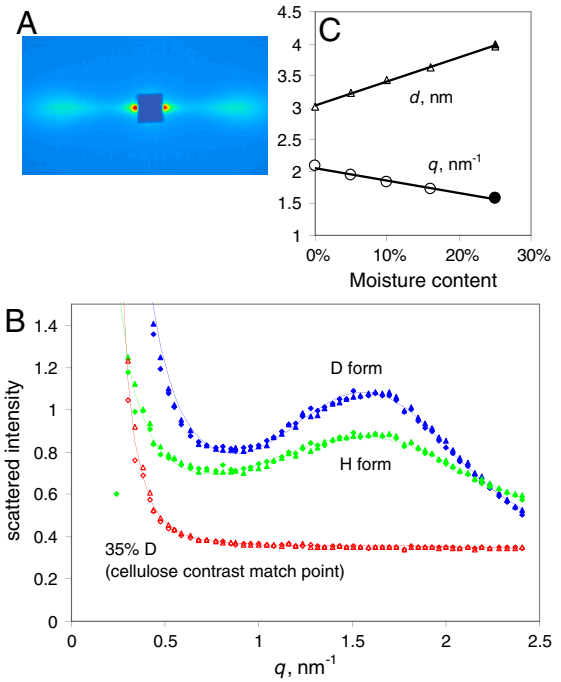

Fig. 1. SANS from spruce wood. (*A*). SANS pattern at 25% hydration with D_2O, showing equatorial Bragg reflections at $q = 1.6$ nm^{-1}. The fiber axis is vertical. (*B*). Radial profiles of SANS intensity at 25% hydration with D_2O, H_2O and a 35:65 mixture of D_2O with H_2O, matching the scattering length density of cellulose based on its elemental composition. (*C*). Variation in position of the center of the fitted radial intensity peak with the level of hydration with D_2O, and the corresponding d-spacings between microfibril centers.

and became zero in 35:65 D_2O:H_2O mixture (Fig. 1). No detectable features were observed on the fiber axis.

When the D_2O content of the wood was reduced from the saturation point of 0.25 g/g the position of the lateral interference peak moved to higher q (Fig. 1) and its intensity diminished. In fully dry spruce wood exchanged with D_2O the interference peak was just discernible at $q = 2.1$ nm^{-1} but it was absent from the scattering pattern from dry wood in the H form. The corresponding mean center-to-center spacings were from 3.0 nm in the dry state to 4.0 nm when saturated with either H_2O or D_2O.

These observations imply that drying reduced the microfibril spacing as H_2O or D_2O was removed, until the microfibrils were packed so densely in the dry H state that there was insufficient contrasting material (or space) to permit measurable interference, whereas in the dry D state deuterium exchange left sufficient deuteroxyl groups at each microfibril surface to provide a small amount of contrast with the H-rich microfibril interior.

Microfibril Dimensions and Disorder: Wide-Angle X-Ray Scattering (WAXS). X-ray diffraction patterns from wood with very well oriented microfibrils resemble the fiber diffraction pattern from crystalline cellulose Iα and Iβ but are much more diffuse (19, 23, 39). At such a low level of resolution it is not possible to distinguish the Iα and Iβ forms by crystallographic means (45) and for clarity all reflections are indexed here on the Iβ lattice. The radial width of the 200 reflection, corresponding to the intersheet spacing in cellulose Iβ, has been widely used as a guide to the diameter of the crystalline part of the microfibril through the Scherrer equation which relates peak broadening inversely to the number of diffracting lattice planes (13, 19, 39). The dimension so obtained is in one direction only, at 90° to the ring planes, and even in that direction it may differ from the true diameter for two reasons. First, the Scherrer dimension represents not the overall diameter but the weighted-mean column length in the direction normal to the lattice plane concerned, and thus depends on the

shape of the microfibril. Also, peak broadening depends on disorder as well as on small lattice dimensions. Radial disorder in cellulose, although its existence is inferred from NMR data (4, 6, 13, 28), is difficult to estimate quantitatively. The radial profile of each reflection contains information on the nature and extent of disorder (46) but in practice the asymmetry of the radial profiles means that most of the available models do not fit well. We introduced an asymmetry term to account for part of the disorder and then modeled the remaining disorder as follows.

If the 400 reflection can be measured, it is possible to correct for disorder-related broadening by assuming that the amount of broadening depends on the square of the reflection order (47). With this correction (Fig. 2) a mean column length of 3.29 ± 0.13 nm normal to the (200) plane was calculated for native spruce wood samples in the dry state, or 2.93 ± 0.05 nm when saturated with water ($n = 4$ in each case). In the diffraction patterns from wood cellulose the 1–10 and 110 reflections overlap strongly. The spacing between centers is controlled by the monoclinic angle γ of the cellulose Iβ lattice (or the corresponding angle in the triclinic Iα lattice) so that it is difficult to extract the widths of these reflections and γ simultaneously. Taking advantage of the fact that γ increases on hydration (36), we recorded diffraction patterns from water-saturated wood samples in which the 1–10 and 110 reflections were centered just far enough apart to be characterized independently (Fig. 2). Allowing for the asymmetry of the reflection profiles γ was determined as $101° \pm 0.5°$ at saturation, greater than the maximum value calculated previously (36). Assuming that both reflections were of equal width and applying the same disorder correction as for the 200 reflection, the mean Scherrer dimension normal to the (1–10) and (110) planes was 2.6 ± 0.1 nm ($n = 4$).

The reduced (200) column length on hydration might suggest that surface chains became detached or disordered, but should be interpreted with caution because these data are sensitive to the background correction, and the backgrounds were much more intense and more complex from wood samples in the wet state. The (200) column lengths for dry samples were slightly greater than reported (without correction for disorder) by Andersson, et al. (19) and considerably greater than reported by Jakob, et al. (23).

The use of an asymmetric model for the reflection profiles permitted much better fits to the observed data than have previously been obtained (Fig. 2), but the accuracy of the Scherrer dimensions is likely to be reduced by a number of approximations that are not reflected in the standard deviations quoted. In particular, deviations from the Bragg equation, and apparently also from the Scherrer equation, become significant in lattices with as few crystal planes as those examined here (48). Also the above value for the mean of the dimensions in the directions normal to (1–10) and (110) depends on the assumption that the disorder parameter is the same in all radial directions; and all estimates of radial broadening, even that of the 200 reflection, depend strongly on the function assumed for the noncrystalline background. We used a background function measured in the region away from the equator, whereas others have derived model backgrounds from disordered materials such as lignin (19, 49) or joined minima in the radial profiles (36).

The Iα and Iβ crystalline forms differ in the longitudinal stagger between successive sheets of chains (50). The (102) lattice plane (as indexed on the Iβ structure) follows this stagger. A line normal to this plane would be interrupted, and the corresponding Scherrer dimension would then be reduced, if any transition between the two crystalline forms were present across a single microfibril. Using the 3.3 nm Scherrer dimension calculated from the 200 reflection and an estimated axial dimension of about 11 nm calculated from the width of the 004 reflection uncorrected for disorder, the predicted Scherrer dimension for the 102 reflection was 5.4 nm when calculated as described (23). However the observed width of the 102 reflection corresponded to a Scherrer dimension of only 3.6 nm, suggesting that there was significant disorder in the intersheet stagger that differentiates the Iα and Iβ lattices.

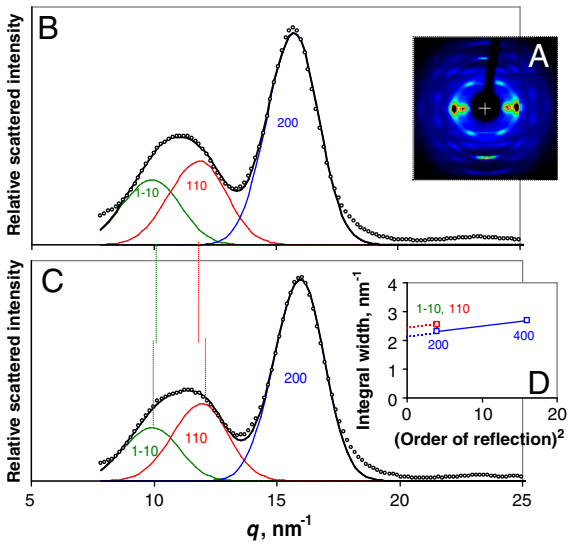

Fig. 2. Wide-angle X-ray scattering from spruce wood. (*A*). WAXS pattern from dry spruce wood. (*B*). Background-corrected equatorial WAXS profiles from dry spruce wood with the 1–10, 110, and 200 reflections fitted by asymmetric functions, using the approximation that the widths of the overlapping 1–10 and 110 reflections were equal. (*C*). Background-corrected equatorial WAXS profiles from hydrated spruce wood, processed as (*B*). (*D*). Variation of the widths of the equatorial reflections with the square of the reflection order. The slope of the line connecting the widths of the 200 and 400 reflections depends on the mean value of the disorder factor and its intercept approximates to the disorder-corrected width. In the absence of measurable higher-order reflections the intercept was estimated for the 1–10 and 110 reflections using the same slope.

C-6 Conformation and Local Mobility from ^{13}C NMR Experiments. The ^{13}C cross polarization, magic-angle spinning (CP-MAS) NMR spectrum from spruce wood (Fig. 3) resembled those obtained from other conifers (6) with distinct groups of C-4 and C-6 signals from well-ordered and disordered cellulose, the latter in particular being overlapped by hemicellulose signals. In ^{13}C spectra from highly crystalline cellulose the Iα and Iβ forms are readily distinguished by the position of their C-4 doublets in the 89 ppm region. In wood spectra the C-4 doublets merge with an intermediate signal that has been attributed to "paracrystalline" cellulose (7). Including this intermediate signal the signal intensity from well ordered cellulose amounted to about 40% of the C-4 total, but precise estimation was difficult due to overlap with hemicellulose signals in the 82–84 ppm region.

In partially ordered solids ^{13}C spin-lattice relaxation times (^{13}C T_1), are a measure of local thermal motion on the 10^{-8} s time scale, and are therefore useful in distinguishing rigid and flexible parts of nanoscale structures. Here, ^{13}C T_1 relaxation times were measured using the MOST (Measurement of Short T_1s) saturation experiment (28, 51). Any ^{13}C atoms in less ordered domains with some freedom of movement have short ^{13}C T_1 and their signal intensity builds up quickly with increasing recycle time, whereas ^{13}C atoms in rigidly ordered domains have longer ^{13}C T_1 and their signal intensity builds up more slowly (28). The MOST experiment has been used previously for primary-wall cellulose but only the C-6 signal was then examined (28). Here we extended the recycle times to include all carbon atoms.

The MOST experiment is only suitable for isolated cellulose, not for intact wood samples where signals originating from more mobile cellulose domains would be swamped by hemicellulose signals. Structural changes during isolation of the cellulose were

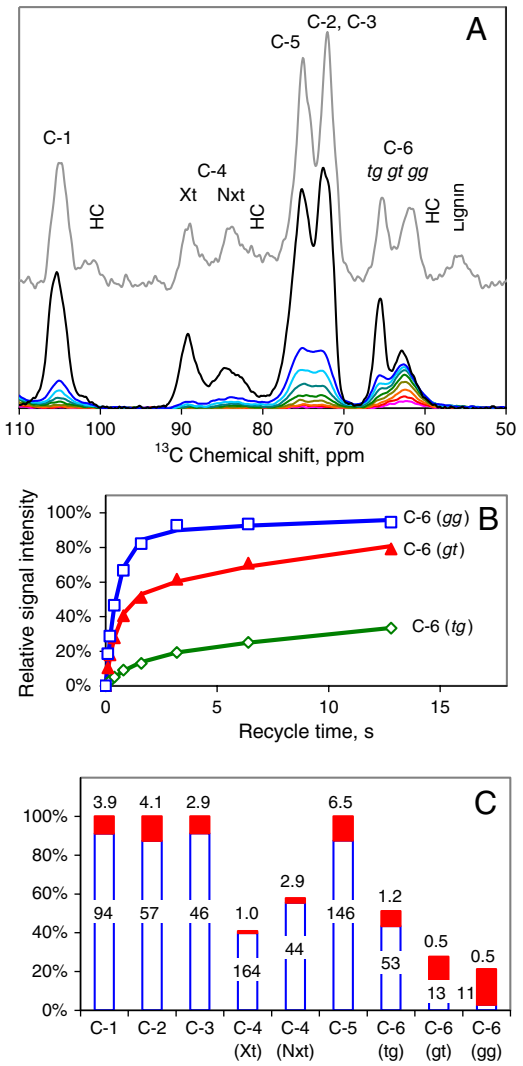

Fig. 3. ^{13}C spin-lattice NMR relaxation experiments on spruce cellulose. (*A*). All cellulose chains are represented in the CP-MAS spectra of spruce wood (top spectrum) and cellulose isolated from it (second top). Shortening the recycle times in the MOST experiment restricted the spectral contribution progressively to the most mobile carbon atoms, particularly C-6. The MOST recycle times were (third to bottom) 12.8, 6.4, 3.2, 1.6, 0.8, 0.4, 0.2, and 0.1 s. The scaling of the CP-MAS spectra relative to the MOST spectra is arbitrary. (*B*). Relative intensity of the deconvoluted *tg*, *gt*, and *gg* components of the C-6 signal from isolated spruce cellulose as a function of recycle time in the MOST experiment, with dual-exponential fitted curves. (*C*). Dual-exponential fitted parameters. The histogram shows the proportions of the long-T_1 and short-T_1 components of each signal and the figures are the corresponding T_1 values in s.

therefore an issue. The CP-MAS spectrum from the isolated cellulose (Fig. 3) not only shows the loss of hemicelluloses and lignin but also indicates that a smaller percentage of the cellulose chains were disordered in the isolated cellulose than in the original wood sample, as has been observed when cellulose crystallinity and microfibril diameter increase during pulping (52, 53).

The evolution of signal intensity with recycle time is shown in Fig. 3. The C-1, C-2, C-3, and C-5 signals each contained overlapping contributions from well ordered and disordered cellulose (28). However based on their ^{13}C T_1 each of these signals could be divided into two components (Fig. 3); a major rigid component with ^{13}C T_1 about 1–2 min and a minor mobile component, around 10% of the total, with ^{13}C T_1 about 5 s. Further subdivision was not feasible with the signal:noise ratio available. The 89 ppm group of signals corresponding to C-4 in well ordered forms of cellulose showed a uniformly long ^{13}C T_1 of nearly 2 min. The MOST experiment is not well suited to such long T_1 values but within the limitations of signal: noise there was no sign of components greater or less in mobility within this group of signals (Fig. 3). Most of the signal intensity centered on 84 ppm, assigned to C-4 in disordered forms of cellulose, showed slightly more mobility than the 89 ppm signals but a minor fraction was much more mobile with ^{13}C T_1 around 3 s.

Judging from the mobility of the ring carbons C-1 to C-5, >90% of the cellulose chains were rather rigid, including disordered as well as ordered forms. In contrast to these ring carbon atoms, C-6 has some freedom to rotate between the *tg*, *gt*, and *gg* conformers unless restrained by stable hydrogen bonding (54). Rotational freedom means that the mobility of C-6 is greater and that each C-6 conformer potentially gives a separate signal. The Iα and Iβ crystalline forms of cellulose have C-6 fixed in the *tg* conformation (9–11).

Fitting a two-component curve to each of these C-6 signals yielded several groups of ^{13}C T_1 values (Fig. 3). The major component of the signal from the *tg* conformer had a long ^{13}C T_1 comparable with the rigid component of the ring carbons and consistent with a crystal-lattice location. This rigid *tg* fraction amounted to 40% of the total C-6 signal. The remainder of the C-6 signal intensity can therefore be assigned to less ordered forms of cellulose, but these varied in mobility. About half of the *gt* signal and a minor fraction of the *gg* signal had ^{13}C T_1 values around 10 s indicating moderate mobility. The remainder of the *gt* signal, most of the *gg* signal, and a small fraction of the *tg* signal had ^{13}C T_1 values of about 1 s or less indicating high mobility.

The MOST data make it clear that motions of the main cellulose chain must be distinguished from C-6 rotation. In total about 40% of the C-6 signal, including all three conformers, showed strong signs of rotational motion and a further 20%, mainly in the *gt* conformation, showed clear but more restricted motion. In contrast significant main-chain motion was restricted to <10% of the cellulose, all within the disordered fraction. Thus a substantial proportion of disordered chains were relatively immobile except for rotation of C-6, which appeared to be permitted by hydrogen-bonding environments less ordered than those found in crystalline cellulose. The *gg* conformer at C-6 predominated in the most mobile environments and the *gt* conformer in environments with somewhat less mobility.

These data refer to the isolated cellulose in which the disordered chains comprised a smaller fraction of the total cellulose than in the intact wood cell walls. However all the same C-4 and C-6 signals were present in the CP-MAS spectrum of spruce wood, at slightly different relative intensities, and it is reasonable to suppose that the associated mobilities were similar in relative terms.

Relative Locations of Polymer Domains: ^1H Spin-Diffusion Experiments. Information on the spatial disposition of cell-wall polymers can be extracted from NMR experiments measuring proton spin diffusion (15, 55, 56). Proton magnetization gradients are first set up by allowing partial spin relaxation, which occurs at different rates in rigid and mobile domains. The proton magnetization is then allowed to reequilibrate between domains by spin diffusion and measured through the ^{13}C spectrum. The length of time required for proton spin diffusion between two domains depends on the square of the distance between them (55, 56).

Results from experiments of this type are normally represented as curves of local magnetization evolving with spin diffusion time and converging when initially distinct domains equilibrate (15). The area enclosed between two such equilibration curves should in principle provide the basis for a two-dimensional (2D) representation of the experiment, in which cross peaks would represent spatially distant pairs of domains. Fig. 4 shows the 2D representation of such an experiment on hydrated spruce early wood, using ^1H spin-spin relaxation to set up the initial magnetization

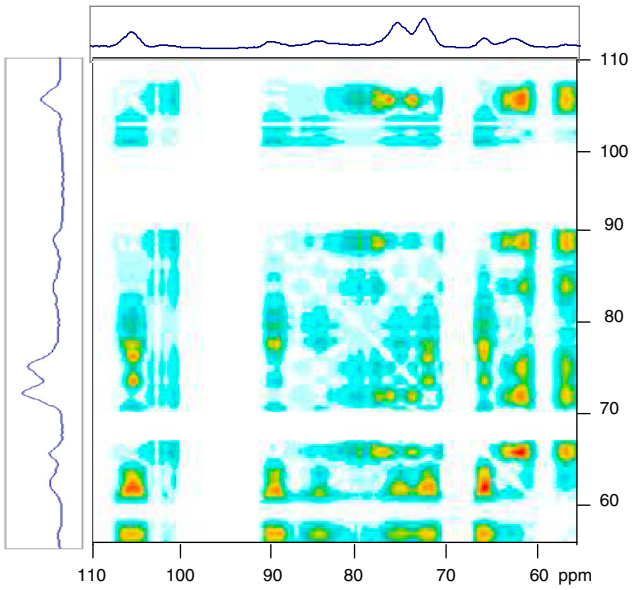

Fig. 4. 2D representation of spectral data from a proton spin-diffusion experiment on hydrated spruce wood. The ^{13}C spectra are shown at top and side. Cross peaks correspond to the relative area enclosed between the T_1-corrected spin equilibration curves for the signals at the two chemical shifts concerned. For a cross peak to be generated between two ^{13}C signals the initial levels of proton magnetization around the two ^{13}C nuclei must differ and significant time must elapse before they equilibrate by proton spin diffusion. That is, the two ^{13}C nuclei must be spatially separated.

gradient. Under these conditions the principal initial reservoirs of magnetization are water molecules and mobile hydrated polymers (56). Late wood gave a similar 2D spectrum (Fig. S1*A*). An experiment in which ^1H rotating-frame spin-lattice relaxation was used gave a similar but less well defined 2D spectrum (Fig. S1*B*). Each cross peak in Fig. 4 corresponds to the signals from ^{13}C atoms in two domains that differed in initial magnetization and were sufficiently separated from one another to require a measurable time (several ms) for spin diffusion to restore their magnetization to equality.

Three groups of signals can be identified in the 2D spectrum (Fig. 4): (a) signals assigned to well-ordered cellulose at 105, **89**, 75, 72, and **66** ppm; (b) signals assigned to conformationally disordered cellulose at 105, **84**, 75, 72, 63, and 61 ppm; and (c) signals assigned to hemicelluloses and lignin at **101**, **80**, 70, and 61 ppm (hemicelluloses) and **56** ppm (lignin). Signals in bold are specific for the group to which they belong, although clearly there is overlap between these groups. Within each group there were no cross peaks. Cross peaks between group (a) and group (b) were weak as expected from the rather small difference in initial magnetization between well-ordered and disordered cellulose. Cross peaks from group (c) to group (a) were considerably stronger, relative to the peak intensities, than cross peaks from group (c) to group (b). This finding implies that, on average, the disordered cellulose was closer than well-ordered cellulose to lignin, hemicelluloses, and water.

With respect to their cross peaks to group (c), there was no sign of any difference between individual regions of the 89 ppm cluster assignable to C-4 in cellulose Iα and Iβ. The implication is not that these crystalline forms, if distinct, occupied domains close to one another, but simply that they were at similar average distances from the nearest water molecules or lignin-hemicellulose domains. The behavior of the central part of the 89 ppm cluster, assigned to "paracrystalline" cellulose (7) was consistent with its inclusion along with material resembling cellulose Iα and Iβ in the well ordered fraction and its cross peaks with the C-6 region of the spectrum indicated a *tg* conformation.

The 2D spectra are not easily reconciled with models in which each microfibril has crystalline and noncrystalline domains alternating along its length (57) because these would be at similar distances from the lignin-hemicellulose matrix in contradiction to our observations. Nor are the 2D spectra consistent with models in which the Iα and Iβ crystalline forms are concentric (4, 56). The results were consistent with a model in which well ordered cellulose forms the core of each microfibril and much of the less ordered cellulose is at the surface, as has been suggested previously on the basis of NMR experiments (6, 15, 58).

Accessibility to Water: Deuteration-FTIR. Cellulose chains accessible to water can be identified by vapor-phase deuterium exchange (28). The OH groups on C-2, C-3, and C-6 of chains accessible to hydration are replaced by OD, as are hemicellulosic OH groups. The O-H stretching bands around 3,300 cm^{-1} in the FTIR spectrum are replaced by O-D stretching bands around 2,500 cm^{-1} (28, 59), allowing the degree of accessibility to water to be measured and revealing the hydrogen-bonding pattern in the water-inaccessible domains.

The intensity removed from the O-H stretching region by deuteration was in a clearly defined band centered on 3,440 cm^{-1} and tailing in the direction of lower frequency. A corresponding band appeared in the O-D stretching region with its maximum at 2,530 cm^{-1} and slight longitudinal polarization (Fig. 5). These bands corresponded to exchangeable hydroxyl groups on hemicelluloses and water-accessible cellulose surfaces and signified a hydrogen-bonding pattern completely different from crystalline cellulose, with lower mean hydrogen-bond strength and near-random hydroxyl orientation. The extent of deuterium exchange at saturation, using a presoak with liquid D_2O followed by drying in rigorously dry air (Fig. S2), amounted to 45% ± 2% of the total hydroxyl groups ($n = 3$). When allowance was made for deuteration of hemicelluloses it could be calculated that 28% of the cellulosic hydroxyl groups were exchangeable. An edge-bound surface chain exchanges the hydroxyls on its outer side only (60), so approximately 56% of the cellulose chains had their outer edges accessible in this way in D_2O-saturated wood.

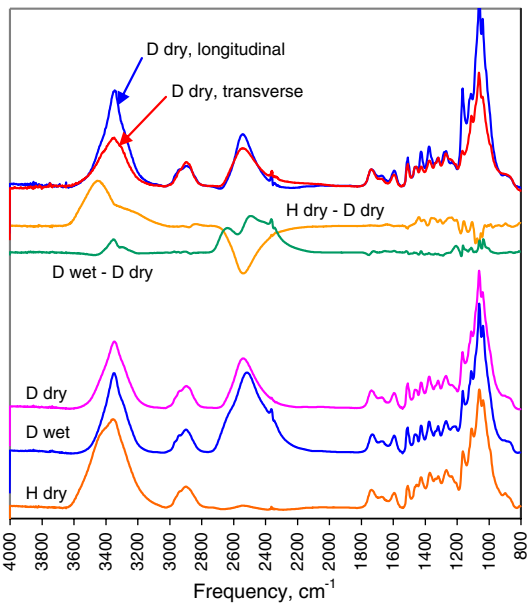

Fig. 5. Baseline-corrected transmission FTIR spectra of spruce wood. From bottom; in the dry state (H dry), then equilibrated with D_2O (D wet) and then dried without access to H_2O (D dry). Deuteration moved the O-H stretching bands from accessible hydroxyl groups (3,200–3,500 cm^{-1}) to the O-D stretching region (2,300–2,600 cm^{-1}). Difference spectra show effects of deuteration (H dry—D dry) and of drying in the deuterated state (D wet—D dry). Top: polarized spectra after deuteration and drying.

When the presoak was omitted the amount of D_2O absorbed from the D_2O-saturated vapor-phase was slightly less than the saturation level and the extent of deuterium exchange was smaller and more variable, as has been noted (61). When the D_2O-saturated wood cell walls were dried there was a minor redistribution of O-H stretching intensity from the crystalline to the noncrystalline pattern. This effect is attributed to a slight distortion of the structure caused by drying stresses.

The residual O-H stretching intensity from cellulose chains inaccessible to water included the longitudinally polarized peak at 3,340 cm^{-1} assigned to O-3 hydrogen bonded to O-5' as in crystalline cellulose Iα and Iβ, but the flanking intensity assigned to O2-H and O6-H stretching vibrations was much more diffuse than in these crystalline forms (Fig. 5). In particular, there was little sign of the sharp, longitudinally oriented bands at 3,240 and 3,270 cm^{-1}, characteristic of the dominant hydrogen-bonding systems between O2 and O6 of successive glucosyl units in the same chain of, respectively, cellulose Iα and cellulose Iβ (28, 62). These two bands were dispersed within a broad, longitudinally polarized shoulder.

Discussion

Relative Abundance of Crystalline and Disordered Domains. How much of the spruce cellulose was "crystalline" depends on how crystalline cellulose is defined or, more realistically, on how it is measured. ^{13}C NMR is sensitive to the conformation of individual chains. WAXS is principally sensitive to how the chains are oriented and how regularly they are packed together within the microfibril. FTIR is sensitive to the hydrogen-bonding patterns that provide cohesion to the chain packing. Data on highly crystalline algal or tunicate celluloses have been obtained by all these methods (6, 9, 10, 59). In principle any such method could be used to define and quantify crystalline cellulose in spruce wood as cellulose similar to algal or tunicate cellulose. However the resemblance was never exact and the criteria for crystallinity differ so much from one method to another that agreement is not to be expected (20).

The CP-MAS NMR spectra indicated that about 40% of the cellulose chains could loosely be called cellulose I, with flat-ribbon chains and C-6 in the *tg* conformation. This fraction includes the form that has been called paracrystalline (7) as well as forms resembling cellulose Iα and Iβ. The remaining 60% with different conformations identifiable by NMR approximately matched in abundance (about 56%) the water-accessible surface chains engaged, on their outer sides, in hydrogen-bonding patterns clearly distinguishable from crystalline cellulose by FTIR. The NMR spin-diffusion data were consistent with a predominantly surface location for these chains. Close proximity of the water accessible and inaccessible chains is implied by deuterium exchange between these under the stress of drying. This finding would not be expected if, for example, water-accessible and inaccessible domains alternated along the length of the microfibril.

Estimating the percentage of crystalline cellulose from WAXS data is problematic, for example due to the difficulty of finding an appropriate "amorphous" calibration standard (49). From the nature of the crystallographic disorder in spruce cellulose it is evident that crystalline merges into disordered and both contribute to the diffraction patterns. The proportion of crystalline cellulose in spruce wood has been estimated at 30% (19), equivalent to about 60% of the total cellulose. This fraction appears to be more than the 40% of cellulose I as defined conformationally by NMR as described above. Both measurements are approximations, but the implication is that at least some of the conformationally disordered chains are located close enough to the corresponding lattice points, and are in approximately the right axial and rotational orientations, to contribute to the crystalline part of the WAXS pattern even though they differ conformationally.

Structure of Crystalline and Related Domains. From the WAXS data it was deduced that many of the cellulose chains were packed similarly to the Iα and Iβ forms but with considerable statistical disorder. Overall, the asymmetry of the equatorial reflections indicated a tendency to looser packing and in the presence of water the monoclinic angle was greater.

Any attempt to establish the relative abundance of the Iα and Iβ forms within this fraction is made difficult by the inclusion of intermediate material termed paracrystalline (7) [note that this term has a different meaning in diffuse diffraction (47)]. As was found previously (7) much of the C-4 signal intensity around 89 ppm in the NMR spectra was somewhat diffuse and was not assignable to the known cellulose Iα and Iβ doublets. The *tg* conformation at C-6, identified by NMR, can accommodate a number of alternative hydrogen-bonding arrangements involving O2 and O6'. A more or less continuous range of hydrogen-bond geometry spanning across the corresponding spectral region was shown to be present by FTIR. Because the coherence of the (102) lattice plane did not extend to the full distance across each microfibril, it cannot even be demonstrated that any one segment of a microfibril was occupied solely by one of the two crystalline forms. Thus although about 40% of the cellulose might reasonably be classed as cellulose I on the grounds of chain conformation, this fraction contained enough hydrogen-bonding disorder within sheets of chains, and enough stacking disorder between sheets, to make it impracticable to distinguish clearly between the Iα and Iβ forms (45).

Disordered Domains. Almost all the cellulose chains were at least moderately well oriented, as shown by both WAXS and polarized FTIR, but the disordered chains differed in conformation from the well ordered material as previously shown by NMR (5, 13). Mostly the disordered chains retained the O3H-O5' hydrogen bond that ensures chain rigidity, as shown by the hydroxyl stretching region in FTIR, but they had a dynamic mixture of all three possible conformations at C-6. These chains resembled the oriented but disordered cellulose that has been prepared by partial dissolution in LiCl/DMAc (63, 64).

On the outer edges of chains accessible enough for D_2O exchange, as in the hemicelluloses, the hydrogen bonding was almost randomly oriented and on average weaker than in crystalline cellulose or liquid water. All three C-6 conformers were present in comparable abundance and probably in dynamic equilibrium, at least in the most mobile fraction of the isolated cellulose. However only a small fraction of this material showed significant mobility of the whole cellulose chain. The *gt* conformation at C-6 predominated in a further fraction with lower mobility that may be tentatively identified with the inner edges of surface chains.

Transverse Dimensions of Microfibrils. It was not, strictly, the microfibril diameter that was obtained from the SANS and WAXS experiments. The SANS experiment yielded a range of center-to-center distances, culminating in a mean minimum distance of 3.0 nm assumed to represent lateral contact in the dry state. On a simple circular model, a diameter of 3.0 nm gives a cross sectional area sufficient for 22 chains packed as in cellulose Iβ.

The WAXS experiments yielded Scherrer column lengths in three transverse directions, that is the dimension in each of these directions averaged across the orthogonal width of the microfibril. Constructing models from these data requires assumptions about the shape of the microfibrils. Microfibrils of, for example, the highly crystalline cellulose from *Valonia* have the (110) and (1–10) crystal faces exposed (60, 65) (for clarity the cellulose Iβ lattice notation is used here even though cellulose Iα predominates in *Valonia* cellulose). Here this shape is called the "diamond" shape whereas an alternative with the (200) and (010) faces exposed is called a "rectangular" shape. It has usually been assumed that the smaller microfibrils of cellulose from higher plants share the diamond shape found in more crystalline celluloses.

Based on this assumption, two distinct ^{13}C T_1 values for the 84 ppm C-4 doublet in the NMR spectrum have been assigned to the exposed (1–10) and (110) faces (6) and simulated in MD studies (66), even though *Valonia* cellulose is now known to give a more complex group of four signals in the 84 ppm region (67). However Family 1 cellulose binding domains bind to cellulose in coniferous wood (68) and *Arabidopsis* secondary cell walls (69) through a planar hydrophobic binding region that is specific for the (200) face when these proteins bind to crystalline celluloses (70) [again we use the Iβ indexing: the same face is indexed as (110) on the Iα lattice]. These findings suggest that cellulose microfibrils in higher plants may have the (200) faces exposed as in the rectangular model, contrary to what has often been assumed.

Initial model-building trials using the mean d-spacings and the measured monoclinic angle from the WAXS images showed that the diamond shape gave smaller column lengths normal to the (200) plane than the mean column length normal to the (110) and (1–10) planes. This relationship was indeed observed for *Valonia* cellulose (Fig. S3). However for water-saturated spruce cellulose the observed column lengths were 2.9 nm normal to the (200) plane and a mean of 2.6 nm normal to the (110) and (1–10) planes. In the dry state the 200 Scherrer dimension increased to 3.3 nm, probably due to either coalescence of partially detached chains or some degree of crystallographic stacking of adjacent microfibrils over short lengths where the 200 planes were aligned.

The column lengths for the wet state could not be matched by the diamond shape but were matched by the rectangular shape (Fig. 6) if the dimensions parallel and orthogonal to the (200) plane were chosen appropriately. Our diffraction data therefore favored the rectangular shape, but should be viewed with caution because disorder may not be rotationally symmetric and because deviations from the Scherrer equation may be observed in such small crystallites (48). The two model structures shown in Fig. 6 have 24 chains, based on the common assumption that the chain number is fixed and divisible by six to match the symmetry of the terminal complex. If not, these models might represent mean structures. An alternative 18-chain model with additional glucomannan chains would fit the SANS data but would be a poorer match to the WAXS data.

Microfibril diameters are calculated from NMR estimates of surface area (20, 71) by assuming that all disordered chains are at the surface and that the mean thickness of the surface monolayer is 0.56 nm, averaged from the (110) and (1–10) d-spacings of cellulose Iβ (9). But a monolayer exposed at the (010) face in the rectangular model would be 0.82 nm thick, and these dimensions may in any case be altered by disorder. We therefore avoided this approach to deducing absolute diameters, although trends calculated in this way agree with other methods (20). Both 24-chain models have over 60% of the chains at hydrophilic surfaces. If these surface chains were mostly disordered as defined by NMR there would be little scope for further disordered cellulose in the microfibril core, but localized discontinuities, at least, must exist at chain ends. Assuming DP = 10,000 (72) there is one such discontinuity on average per 200 nm of a 24-chain microfibril. Spruce cellulose when hydrolyzed with sulphuric acid breaks down into whiskers 200–400 nm long, with significant simultaneous loss of noncrystalline material assumed to come from extensive, acid-labile amorphous segments between them (73). However localized regions of disorder at chain ends might be sufficient to initiate acid cleavage of microfibrils, with disordered surface cellulose being hydrolyzed or crystallized independently.

The comparison between wood and primary-wall cellulose is of interest. Primary-wall microfibrils from celery collenchyma are about 3 nm in diameter as estimated by methods similar to those used here (28, 41). Other primary-wall microfibrils are either similar (74) or smaller (31, 71, 74) in diameter. C-6 conformations and H-bonding patterns in the disordered fraction of celery cellulose (28) were qualitatively similar to those reported here

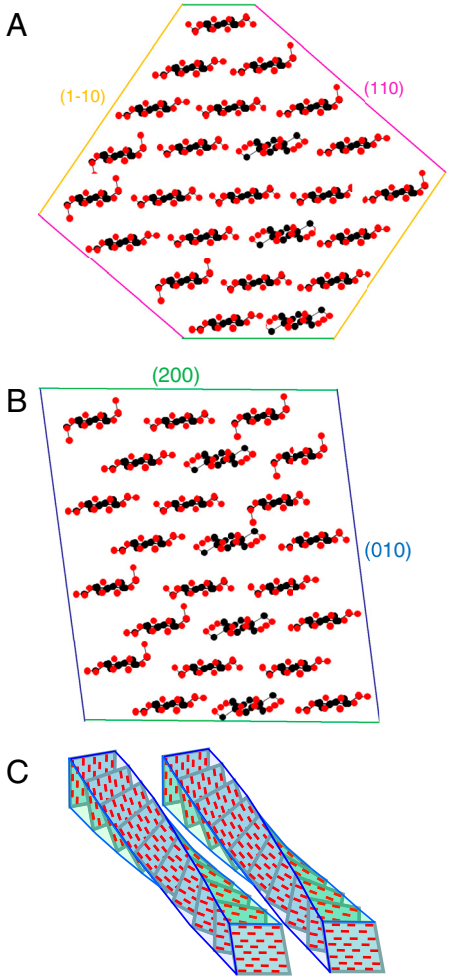

Fig. 6. Chain packing arrangements for alternative shapes of spruce cellulose microfibrils. (*A*). Diamond shape. 24 chains, overall dimensions 3.2 × 3.9 nm. Weighted-mean column lengths normal to lattice planes (002), 2.7 nm; (1–10), 3.2 nm, (110), 2.6 nm. (*B*). Rectangular shape. 24 chains, overall dimensions 3.2 × 3.1 nm. Weighted-mean column lengths normal to lattice planes (002), 3.2 nm; (1–10), 2.8 nm, (110), 2.5 nm. Shape (*B*) is in closer accord with the observed Scherrer dimensions corrected for disorder. (*C*) Schematic diagram of two adjacent twisted microfibrils. Even if they have the same helical pitch, the ability of any crystal face to bind against the corresponding crystal face in the next microfibril is progressively lost with distance along the microfibril axis.

but primary-wall celluloses show consistent crystallographic differences, particularly the reduced monoclinic angle that has led these celluloses to be described as cellulose IV (48).

Axial Coherence and Twist. It has been suggested that alternation between crystalline and disordered segments defines the length over which longitudinal crystallographic coherence is maintained. This length was only about 11 nm in the present experiments, uncorrected for disorder. Published axial Scherrer dimensions vary (19) as the width of the 004 reflection is often little greater than the instrumental broadening, but this dimension is clearly less than the length of nanocrystals prepared from wood cellulose (75) or isolated single sheets of chains (30). Some other feature must therefore contribute to the loss of axial coherence.

Considering how little variation is reported in the c dimension of the unit cell (19, 23, 76), the most likely contributor is twisting of the microfibril, which has been observed (3, 77–79) and simulated by MD (54), but see ref. 80. The mean helical pitch would probably need to be at least an order of magnitude greater than the resulting column length and would therefore be too long to

give rise to small-angle axial scattering features within the q range of our SANS experiments.

Microfibril Aggregation. The SANS data for dry spruce cellulose clearly demonstrated aggregation of microfibrils into larger units. Both the SANS and the FTIR experiments showed that at increasing moisture content, increasing amounts of water penetrated between the microfibrils within each aggregate. The data implied the separation of some segments by up to about 1 nm (4.0 nm-3.0 nm) at 25% D_2O by mass, but if all microfibrils were at this spacing it would imply a greater volume increase on hydration than is known to take place. More probably spacings were irregular (3) and the coherent SANS intensity was dominated by spacings greater than the mean, because the SANS contrast is expected to be greater for well separated pairs of microfibrils with D_2O between them.

Penetration of water into microfibril aggregates was unexpected, because aggregation of microfibrils was first suggested on the evidence that cellulose surfaces within such aggregates were inaccessible to solvents (6). But the solvents concerned did not include water, and water has much greater ability to separate and dissolve polysaccharide chains than, for example, the lower alcohols. Most of the outward-facing hydroxyl groups on the microfibril surfaces appeared to be accessible to deuterium exchange at saturation, although in the presence of smaller amounts of water many of the interfaces between microfibrils clearly remained dry. As the exchange process was probably dynamic it does not imply that a layer of water was permanently interposed between microfibrils, nor that the cohesion of the aggregates was completely disrupted, but only that water molecules could penetrate between microfibrils over some of their length in the hydrated state.

Conclusions

Our data suggest microfibrils with about 24 chains, possibly twisted and with considerable disorder increasing towards the surfaces. Less extensive disordered regions probably exist within the core of each microfibril. Tight lateral binding is facilitated by the hydrogen-bonding pattern of the surface chains, at only a small cost in tensile stiffness due to the loss of intramolecular hydrogen bonding between O2 and O6 (81). The surface location of these disordered chains means that a parallel mechanical model with tight lateral bonding to the ordered core is more appropriate than a series model, consistent with FTIR observations (35). The twisting of adjacent microfibrils may explain why they do not come into crystallographic register with one another over enough of their length to coalesce.

It is not certain that the number of chains in one microfibril is fixed and corresponds to the number synthesized by one terminal complex (27, 31), but if so each lobe of the terminal complex would be likely to synthesise four chains rather than six as has been assumed. As it travels through the cell membrane the terminal complex would seem to have to rotate, so that it leaves the microfibril twisted behind it (32). Rotation of densely arrayed terminal complexes might lead to mechanical interference between them with implications for the parallel, oriented deposition required for morphogenesis of secondary plant tissues (32, 33).

A rectangular model is favored for spruce microfibrils, differing from more crystalline celluloses in having one hydrophobic and one hydrophilic face exposed (54). It is not clear how other polymers restrict access of cellulases to the hydrophobic surfaces, but impacts of the structure and aggregation of microfibrils on the recalcitrance of woody biomass are to be expected (82).

Materials and Methods

Materials. Mature earlywood from Sitka spruce [*Picea sitchensis* (Bong.) Carr.] was prepared as described (15) and longitudinal-tangential sections 20 μm in thickness were prepared wet on a sledge microtome. A three-stage extraction process (see *SI Text*) was used to isolate cellulose from this material for the NMR relaxation experiment.

SANS. SANS analysis was conducted on beamline D11 at the Institut Laue-Langevin (ILL), Grenoble. Scattered neutrons were detected on a 96×96 cm CERCA ^{3}He gas detector, at a sample-to-detector distance of 2 m and collimation length 8 m. The neutron wavelength was 0.6 nm with a dispersion of 9–10%. The q range covered in this experiment extended from 0.3 nm^{-1} to 2.4 nm^{-1}. Samples 2 mm in thickness were adjusted to the desired moisture content by saturating with H_2O, D_2O, or 35:65 D_2O:H_2O (see *SI Text*) then equilibrating with phosphorus pentoxide and encapsulating in aluminum foil, with an empty foil container used as background.

WAXS. X-ray diffraction patterns were obtained at ambient temperature using a Rigaku R-axis/RAPID image plate diffractometer. A Mo Kα ($\lambda = 0.07071$ nm) source was used, with the beam collimated to a diameter of 0.5 mm. Scattering angles were expressed as $q = 4\pi \sin\theta/\lambda$. Samples were 1 mm or 2 mm thick in the direction parallel to the beam and their other dimensions exceeded the beam diameter. The hydrated samples were saturated with H_2O and then moisture adjusted as above and encapsulated in polyethylene film. The diffraction patterns were collected in perpendicular transmission mode except for tilting experiments to measure the width of the axial reflections. Radial profiles of scattered intensity I as a function of q were integrated over an azimuthal angle of 5° on either side of the equator and meridian, using the AreaMax software package (Rigaku/MSC). See *SI Text* for background correction procedures and fitting of asymmetric peak functions to the equatorial profiles. It was assumed that a plot of peak width F against the square of the order of reflection r^2 is linear (47) with, at the intercept, the Scherrer dimension (mean column length) $L = k\lambda/F\cos\theta$ where the Scherrer constant $k = 0.94$ as appropriate for a cylindrical crystallite.

FTIR Microscopy. Longitudinal-tangential 20 μm sections were used for transmission FTIR spectroscopy with vapor-phase deuterium exchange as described previously (28) (See *SI Text*). For full saturation with D_2O the sample was presoaked with D_2O (1 μL) and the upper window of the cell was immediately replaced, with an uninterrupted flow of D_2O vapor. The data reported here were recorded during experiments in which the OH : OD ratio remained constant for at least 30 min under rigorously dry conditions, much longer than required to collect the spectra (Fig. S2).

Solid-State NMR. CP-MAS spectra were obtained on a Varian VNMRS spectrometer operating at 100.56 MHz for ^{13}C with a MAS rate of 8 kHz and two-pulse phase modulation ^{1}H decoupling at 96.2 kHz. A linear CP ramp was used with contact time 1 ms. Recycle time was 4 s. Spectral referencing was with respect to tetramethylsilane.

Single-pulse-excitation (SP-MAS) ^{13}C NMR spectra were obtained from isolated spruce cellulose using the MOST multiple-pulse proton decoupling sequence (28, 51). See *SI Text* for details.

Spin-diffusion experiments with initial proton magnetization gradient set up using spin-spin relaxation were carried out as reported previously (15). For the derivation of the 2D representation of this experiment see *SI Text*.

ACKNOWLEDGMENTS. We thank Prof J. Sugiyama for helpful comments and the gift of a *Valonia* cellulose sample. The authors acknowledge financial support from the UK Engineering and Physical Science Research Council (Grant EP/E026583/1 and support for the solid-state NMR facility at Durham), the Scottish Funding Council (SIRT Programme Fellowship to C.M.A.), Rigaku Europe (instrument loan), and the Institut Laue-Langevin, Grenoble, France (beamtime support).

1. Dixon RK, et al. (1994) Carbon pools and flux of global forest ecosystems. *Science* 263:185–190.
2. Carroll A, Somerville C (2009) Cellulosic biofuels. *Annu Rev Plant Biol* 60:165–182.
3. Xu P, Donaldson LA, Gergely ZR, Staehelin LA (2007) Dual-axis electron tomography: a new approach for investigating the spatial organization of wood cellulose microfibrils. *Wood Sci Technol* 41:101–116.
4. Atalla RH, Vander Hart DL (1999) The role of solid state C-13 NMR spectroscopy in studies of the nature of native celluloses. *Solid State Nucl Mag* 15:1–19.
5. Vietor RJ, Newman RH, Ha MA, Apperley DC, Jarvis MC (2002) Conformational features of crystal-surface cellulose from higher plants. *Plant J* 30:721–731.
6. Wickholm K, Larsson PT, Iversen T (1998) Assignment of non-crystalline forms in cellulose I by CP/MAS C-13 NMR spectroscopy. *Carbohydr Res* 312:123–129.
7. Larsson PT, Wickholm K, Iversen T (1997) A CP/MAS C-13 NMR investigation of molecular ordering in celluloses. *Carbohydr Res* 302:19–25.
8. Newman RH (1999) Estimation of the relative proportions of cellulose I alpha and I beta in wood by carbon-13 NMR spectroscopy. *Holzforschung* 53:335–340.

9. Nishiyama Y, Langan P, Chanzy H (2002) Crystal structure and hydrogen-bonding system in cellulose 1 beta from synchrotron X-ray and neutron fiber diffraction. *J Am Chem Soc* 124:9074–9082.
10. Nishiyama Y, Sugiyama J, Chanzy H, Langan P (2003) Crystal structure and hydrogen bonding system in cellulose 1(alpha), from synchrotron X-ray and neutron fiber diffraction. *J Am Chem Soc* 125:14300–14306.
11. Nishiyama Y, Johnson GP, French AD, Forsyth VT, Langan P (2008) Neutron crystallography, molecular dynamics, and quantum mechanics studies of the nature of hydrogen bonding in cellulose I-beta. *Biomacromolecules* 9:3133–3140.
12. Kataoka Y, Kondo T (1999) Quantitative analysis for the cellulose I alpha crystalline phase in developing wood cell walls. *Int J Biol Macromol* 24:37–41.
13. Newman RH, Davidson TC (2004) Molecular conformations at the cellulose-water interface. *Cellulose* 11:23–32.
14. Akerholm M, Salmen L (2001) Interactions between wood polymers studied by dynamic FT-IR spectroscopy. *Polymer* 42:963–969.
15. Altaner C, Apperley DC, Jarvis MC (2006) Spatial relationships between polymers in Sitka spruce: Proton spin-diffusion studies. *Holzforschung* 60:665–673.
16. Donaldson L (2007) Cellulose microfibril aggregates and their size variation with cell wall type. *Wood Sci Technol* 41:443–460.
17. Fahlen J, Salmen L (2005) Pore and matrix distribution in the fiber wall revealed by atomic force microscopy and image analysis. *Biomacromolecules* 6:433–438.
18. Zimmermann T, Richter K, Bordeanu N, Sell J (2007) Arrangement of cell-wall constituents in chemically treated Norway spruce tracheids. *Wood Fiber Sci* 39:221–231.
19. Andersson S, Serimaa R, Paakkari T, Saranpaa P, Pesonen E (2003) Crystallinity of wood and the size of cellulose crystallites in Norway spruce (*Picea abies*). *J Wood Sci* 49:531–537.
20. Newman RH (1999) Estimation of the lateral dimensions of cellulose crystallites using C-13 NMR signal strengths. *Solid State Nucl Mag* 15:21–29.
21. Newman RH (2004) Homogeneity in cellulose crystallinity between samples of *Pinus radiata* wood. *Holzforschung* 58:91–96.
22. Peura M, et al. (2008) X-ray microdiffraction reveals the orientation of cellulose microfibrils and the size of cellulose crystallites in single Norway spruce tracheids. *Trees-Struct Funct* 22:49–61.
23. Jakob HF, Fengel D, Tschegg SE, Fratzl P (1995) The elementary cellulose fibril in *Picea abies*: Comparison of transmission electron microscopy, small-angle X-ray scattering, and wide-angle X-ray scattering results. *Macromolecules* 28:8782–8787.
24. Mueller SC, Brown RM (1980) Evidence for an intramembrane component associated with a cellulose microfibril-synthesizing complex in higher plants. *J Cell Biol* 84:315–326.
25. Endler A, Persson S (2011) Cellulose synthases and synthesis in Arabidopsis. *Mol Plant* 4:199–211.
26. Herth W (1983) Arrays of plasma-membrane rosettes involved in cellulose microfibril formation of *Spirogyra*. *Planta* 159:347–356.
27. Ding SY, Himmel ME (2006) The maize primary cell wall microfibril: a new model derived from direct visualization. *J Agric Food Chem* 54:597–606.
28. Sturcova A, His I, Apperley DC, Sugiyama J, Jarvis MC (2004) Structural details of crystalline cellulose from higher plants. *Biomacromolecules* 5:1333–1339.
29. Washusen R, Evans R (2001) The association between cellulose crystallite width and tension wood occurrence in *Eucalyptus globulus*. *IAWA Journal* 22:235–243.
30. Li Q, Renneckar S (2009) Molecularly thin nanoparticles from cellulose: isolation of sub-microfibrillar structures. *Cellulose* 16:1025–1032.
31. Niimura H, Yokoyama T, Kimura S, Matsumoto Y, Kuga S (2010) AFM observation of ultrathin microfibrils in fruit tissues. *Cellulose* 17:13–18.
32. Somerville C (2006) Cellulose synthesis in higher plants. *Annu Rev Cell Dev Bi* 22:53–78.
33. Burgert I, Fratzl P (2009) Plants control the properties and actuation of their organs through the orientation of cellulose fibrils in their cell walls. *Integrative and Comparative Biology* 49:69–79.
34. Kong K, Wilding MA, Ibbett RN, Eichhorn SJ (2008) Molecular and crystal deformation of cellulose: uniform strain or uniform stress? *Faraday Discuss* 139:283–298.
35. Salmen L, Bergstrom E (2009) Cellulose structural arrangement in relation to spectral changes in tensile loading FTIR. *Cellulose* 16:975–982.
36. Zabler S, Paris O, Burgert I, Fratzl P (2010) Moisture changes in the plant cell wall force cellulose crystallites to deform. *J Struct Biol* 171:133–141.
37. Momeni K, Yassar RS (2009) Analytical formulation of stress distribution in cellulose nanocomposites. *J Comput Theor Nanos* 6:1511–1518.
38. Xu P, Liu H (2004) Models of microfibril elastic modulus parallel to the cell axis. *Wood Sci Technol* 38:363–374.
39. Park S, Baker JO, Himmel ME, Parilla PA, Johnson DK (2010) Cellulose crystallinity index: measurement techniques and their impact on interpreting cellulase performance. *Biotechnology for Biofuels* 3:1–10.
40. Hulmes DJS, Wess TJ, Prockop DJ, Fratzl P (1995) Radial packing, order, and disorder in collagen fibrils. *Biophys J* 68:1661–1670.
41. Kennedy CJ, et al. (2007) Microfibril diameter in celery collenchyma cellulose: X-ray scattering and NMR evidence. *Cellulose* 14:235–246.
42. Jungnikl K, Paris O, Fratzl P, Burgert I (2008) The implication of chemical extraction treatments on the cell wall nanostructure of softwood. *Cellulose* 15:407–418.
43. Crawshaw J, Vickers ME, Briggs NP, Heenan RK, Cameron RE (2000) The hydration of TENCEL® cellulose fibres studied using contrast variation in small angle neutron scattering. *Polymer* 41:1873–1881.
44. Kennedy CJ, Sturcova A, Jarvis MC, Wess TJ (2007) Hydration effects on spacing of primary-wall cellulose microfibrils: a small angle X-ray scattering study. *Cellulose* 14:401–408.
45. Wada M, Okano T, Sugiyama J, Horii F (1995) Characterization of tension and normally lignified wood cellulose in *Populus maximowiczii*. *Cellulose* 2:223–233.
46. Samir OM, Somashekar R (2007) Intrinsic strain effect on crystal and molecular structure of (dch32) cotton fiber. *Powder Diffr* 22:20–26.
47. Hindeleh AM, Hosemann R (1991) Microparacrystals—the intermediate stage between crystalline and amorphous. *J Mater Sci* 26:5127–5133.
48. Newman RH (2008) Simulation of X-ray diffractograms relevant to the purported polymorphs cellulose IV_I and IV_{II}. *Cellulose* 15:769–778.
49. Thygesen A, Oddershede J, Lilholt H, Thomsen AB, Stahl K (2005) On the determination of crystallinity and cellulose content in plant fibres. *Cellulose* 12:563–576.
50. Jarvis MC (2000) Interconversion of the I alpha and I beta crystalline forms of cellulose by bending. *Carbohydr Res* 325:150–154.
51. Findlay A, Harris RK (1990) A pulse sequence for the measurement of short spin-lattice relaxation times for C-13 in solid polymers. *Magn Reson Chem* 28:S104–S107.
52. Hult EL, Iversen T, Sugiyama J (2003) Characterization of the supermolecular structure of cellulose in wood pulp fibres. *Cellulose* 10:103–110.
53. Liitia T, et al. (2003) Cellulose crystallinity and ordering of hemicelluloses in pine and birch pulps as revealed by solid-state NMR spectroscopic methods. *Cellulose* 10:307–316.
54. Matthews JF, et al. (2006) Computer simulation studies of microcrystalline cellulose I beta. *Carbohydr Res* 341:138–152.
55. Newman RH (1992) Nuclear magnetic resonance study of spatial relationships between chemical components in wood cell walls. *Holzforschung* 46:205–210.
56. Taylor RE, et al. (2008) H-1 and C-13 solid-state NMR of Gossypium barbadense (Pima) cotton. *J Mol Struct* 878:177–184.
57. Eichhorn SJ, et al. (2010) Review: current international research into cellulose nanofibres and nanocomposites. *J Mater Sci* 45:1–33.
58. Newman RH (1998) Evidence for assignment of C-13 NMR signals to cellulose crystallite surfaces in wood, pulp and isolated celluloses. *Holzforschung* 52:157–159.
59. Marechal Y, Chanzy H (2000) The hydrogen bond network in I-beta cellulose as observed by infrared spectrometry. *J Mol Struct* 523:183–196.
60. Horikawa Y, Clair B, Sugiyama J (2009) Varietal difference in cellulose microfibril dimensions observed by infrared spectroscopy. *Cellulose* 16:1–8.
61. Taniguchi T, Harada H, Nakato K (1978) Determination of water adsorption sites in wood by a hydrogen-deuterium exchange. *Nature* 272:230–231.
62. Schmidt M, Gierlinger N, Schade U, Rogge T, Grunze M (2006) Polarized infrared microspectroscopy of single spruce fibers: hydrogen bonding in wood polymers. *Biopolymers* 83:546–555.
63. Duchemin B, Newman RH, Staiger MP (2007) Phase transformations in microcrystalline cellulose due to partial dissolution. *Cellulose* 14:311–320.
64. Hishikawa Y, Togawa E, Kondo T (2010) Molecular orientation in the nematic ordered cellulose film using polarized FTIR accompanied with a vapor-phase deuteration method. *Cellulose* 17:539–545.
65. Baker AA, Helbert W, Sugiyama J, Miles MJ (1997) High-resolution atomic force microscopy of native *Valonia* cellulose I microcrystals. *J Struct Biol* 119:129–138.
66. Bergenstrahle M, Wohlert J, Larsson PT, Mazeau K, Berglund LA (2008) Dynamics of cellulose-water interfaces: NMR spin-lattice relaxation times calculated from atomistic computer simulations. *J Phys Chem B* 112:2590–2595.
67. Malm E, Bulone V, Wickholm K, Larsson PT, Iversen T (2010) The surface structure of well-ordered native cellulose fibrils in contact with water. *Carbohydr Res* 345:97–100.
68. Kawakubo T, et al. (2010) Analysis of exposed cellulose surfaces in pretreated wood biomass using carbohydrate-binding module (CBM)-cyan fluorescent protein (CFP). *Biotechnol Bioeng* 105:499–508.
69. Blake AW, et al. (2006) Understanding the biological rationale for the diversity of cellulose-directed carbohydrate-binding modules in prokaryotic enzymes. *J Biol Chem* 281:29321–29329.
70. Lehtio J, et al. (2003) The binding specificity and affinity determinants of family 1 and family 3 cellulose binding modules. *Proc Natl Acad Sci USA* 100:484–489.
71. Ha MA, et al. (1998) Fine structure in cellulose microfibrils: NMR evidence from onion and quince. *Plant J* 16:183–190.
72. Schult T, Hjerde T, Inge Optun O, Kleppe PJ, Moe S (2002) Characterization of cellulose by SEC-MALLS. *Cellulose* 9:149–158.
73. Bondeson D, Mathew A, Oksman K (2006) Optimization of the isolation of nanocrystals from microcrystalline cellulose by acid hydrolysis. *Cellulose* 13:171–180.
74. Smith BG, Harris PJ, Melton LD, Newman RH (1998) Crystalline cellulose in hydrated primary cell walls of three monocotyledons and one dicotyledon. *Plant Cell Physiol* 39:711–720.
75. Lahiji RR, et al. (2010) Atomic force microscopy characterization of cellulose nanocrystals. *Langmuir* 26:4480–4488.
76. Davidson TC, Newman RH, Ryan MJ (2004) Variations in the fibre repeat between samples of cellulose I from different sources. *Carbohydr Res* 339:2889–2893.
77. Elazzouzi-Hafraoui S, et al. (2008) The shape and size distribution of crystalline nanoparticles prepared by acid hydrolysis of native cellulose. *Biomacromolecules* 9:57–65.
78. Hanley SJ, Revol JF, Godbout L, Gray DG (1997) Atomic force microscopy and transmission electron microscopy of cellulose from *Micrasterias denticulata*; evidence for a chiral helical microfibril twist. *Cellulose* 4:209–220.
79. Santa-Maria M, Jeoh T (2010) Molecular-scale investigations of cellulose microstructure during enzymatic hydrolysis. *Biomacromolecules* 11:2000–2007.
80. Matthews JF, et al. (2011) High-temperature behavior of cellulose I. *J Phys Chem B* 115:2155–2166.
81. Tashiro K, Kobayashi M (1991) Theoretical evaluation of 3-dimensional elastic constants of native and regenerated celluloses - Role of hydrogen bonds. *Polymer* 32:1516–1530.
82. Himmel ME, et al. (2007) Biomass recalcitrance: engineering plants and enzymes for biofuels production. *Science* 315:804–807.